Ultrasonics Sonochemistry 99 (2023) 106582

Contents lists available at ScienceDirect

Ultrasonics Sonochemistry

journal homepage: www.elsevier.com/locate/ultson

Fabricating carbon quantum dots of graphitic carbon nitride vis ultrasonic exfoliation for highly efficient H_2O_2 production

Yue Wang [a,b], Zhaojing Yang [a], Chengxu Zhang [a], Yuebin Feng [c], Haodong Shao [a,b], Jian Chen [a], Jue Hu [a,b,*], Libo Zhang [a,b,*]

[a] Faculty of Metallurgical and Energy Engineering, Kunming University of Science and Technology, Kunming 650093, China
[b] State Key Laboratory of Complex Nonferrous Metal Resources Clean Utilization, Kunming University of Science and Technology, Kunming 650093, China
[c] Faculty of Science, Kunming University of Science and Technology, Kunming 650093, China

ARTICLE INFO

Keywords:
Graphitic carbon nitride
Ultrasound
Two-electron oxygen reduction
Hydrogen peroxide preparation

ABSTRACT

A promising and sustainable approach for producing hydrogen peroxide is the two-electron oxygen reduction reaction ($2e^-$ ORR), which uses very stable graphitic carbon nitride (g-C_3N_4). However, the catalytic performance of pristine g-C_3N_4 is still far from satisfactory. Here, we demonstrate for the first time the controlled fabrication of carbon quantum dots (CQDs)-modified graphitic carbon nitride carbon (g-C_3N_4/CQDs-X) by ultrasonic stripping for efficient $2e^-$ ORR electrocatalysis. HRTEM, UV–vis, EPR and EIS analyses are in good consistent which prove the in-situ generation of CQDs. The effect of sonication time on the physical properties and ORR activity of g-C_3N_4 is discussed for the first time. The g-C_3N_4/CQDs-12 catalyst shows a selectivity of up to 95% at a potential of 0.35 V vs. RHE, which is much higher than that of the original g-C_3N_4 catalyst (88%). Additionally, the H_2O_2 yield is up to 1466.6 mmol g^{-1} in 12 h, which is twice as high as the original g-C_3N_4 catalyst. It is discovered that the addition of CQDs through ultrasonic improves the g-C_3N_4 catalyst's electrical conductivity and electron transfer capability in addition to its high specific surface area and distinctive porous structure, speeding up the reaction rate. This research offers a green method for enhancing g-C_3N_4 activity.

1. Introduction

Hydrogen peroxide (H_2O_2) is a versatile and environmentally friendly oxidant widely used in bleaching, disinfection, wastewater treatment, chemical synthesis, semiconductor cleaning, and exhaust gas treatment [1]. However, the traditional anthraquinone method dominates H_2O_2 production, which is costly, polluting, and detrimental to the environment and ecological safety. Moreover, the transport of H_2O_2 increases the risk of explosion [2]. Compared with the anthraquinone method, electrocatalytic preparation of H_2O_2 offers a promising, cost-effective method without pollutant emission during synthesis [3]. However, the selectivity for H_2O_2 synthesis during the $2e^-$ ORR process proves challenging because the competing four-electron oxygen reduction mostly generates water. Therefore, it is essential to build catalysts with strong $2e^-$ ORR activity and H_2O_2 selectivity [4]. There have been studies on a variety of $2e^-$ ORR catalysts, including carbon-based materials, noble metals, and their alloys. Even though noble metal alloys like Pd-Au, Pd-Hg, and Pt-Hg have high $2e^-$ ORR selectivity, their cost and unavailability prevent them from being widely used in industry. Presently, metal-free carbon catalysts are favored for their good electrical conductivity, high specific surface area, ease of modification, abundance, and low price [5].

As a developing metal-free polymer catalyst using triazine (C_3N_3) or heptazine (C_6N_7) as the fundamental unit, graphitic-phase carbon nitride (g-C_3N_4), exhibits tremendous potential [6]. As a polymer semiconductor with a sp^2 conjugation system, g-C_3N_4 nanosheets offer a large specific surface area, short charge transfer distance, high solubility, good stability, and a tunable electronic structure [7,8], enabling various applications in photocatalytic hydrolysis, CO_2 conversion, N_2 fixation, pollutant degradation, hydrogen evolution reaction, CO-oxidation reaction and H_2O_2 production [9–19]. However, the yield of catalytic H_2O_2 generated from pristine g-C_3N_4 remains unsatisfactory. Numerous changes have been used to increase the effectiveness and selectivity of H_2O_2 produced from g-C_3N_4, including defect engineering, metal loading, heterostructure building, and morphological management. Among these techniques, morphological alteration of g-C_3N_4 can

* Corresponding authors.
E-mail addresses: hujue@kust.edu.cn (J. Hu), lbzhang@kust.edu.cn (L. Zhang).

https://doi.org/10.1016/j.ultsonch.2023.106582
Received 29 July 2023; Received in revised form 28 August 2023; Accepted 30 August 2023
Available online 1 September 2023

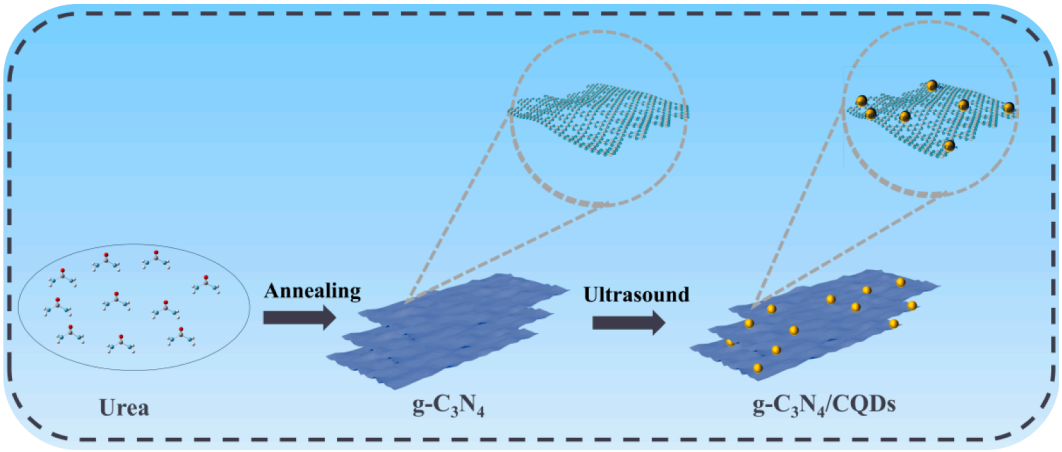

Fig. 1. Preparation process of g-C_3N_4/CQDs.

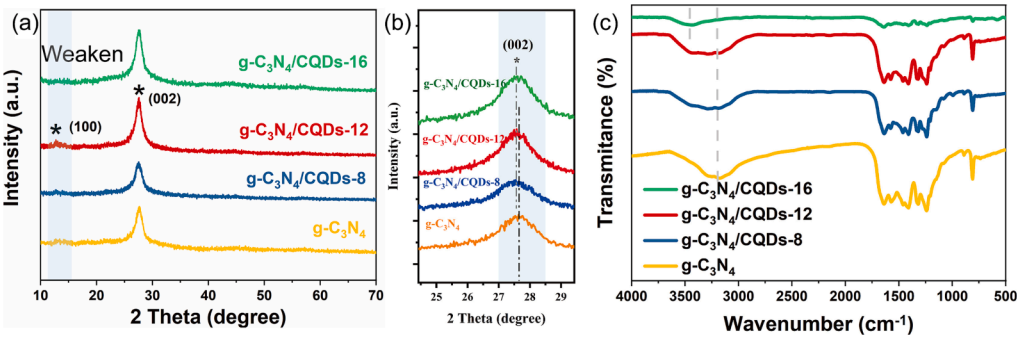

Fig. 2. Complete (a) and (b) enlarged XRD patterns (c) FTIR spectra of g-C_3N_4, g-C_3N_4/CQDs-8, g-C_3N_4/CQDs-12, and g-C_3N_4/CQDs-16.

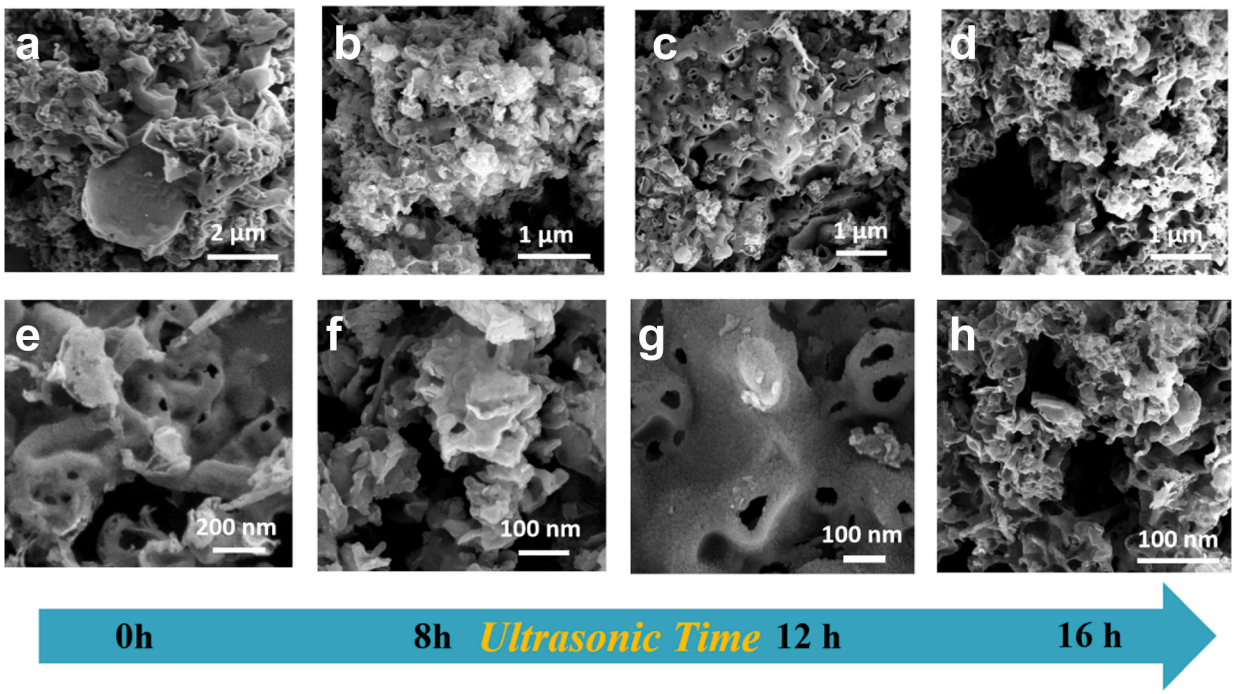

Fig. 3. SEM images under different ultrasonic treatment duration, (a), (e) without ultrasonic treatment; (b), (f) ultrasonic treatment for 8 h; (c), (g) ultrasonic treatment for 12 h; (d), (h) ultrasonic treatment for 16 h.

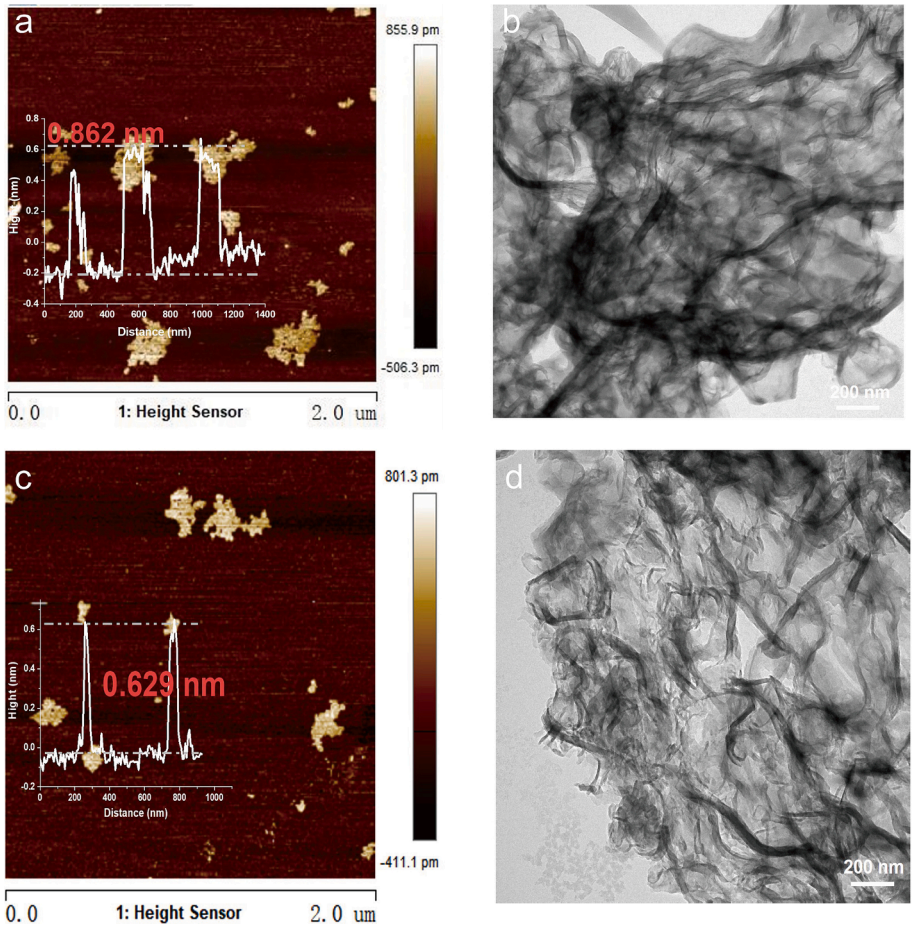

Fig. 4. Contrast before and after exfoliation treatment. AFM images of (a) g-C_3N_4;(c) g-C_3N_4/CQDs-12, TEM images of (b) g-C_3N_4,(d) g-C_3N_4/CQDs-12.

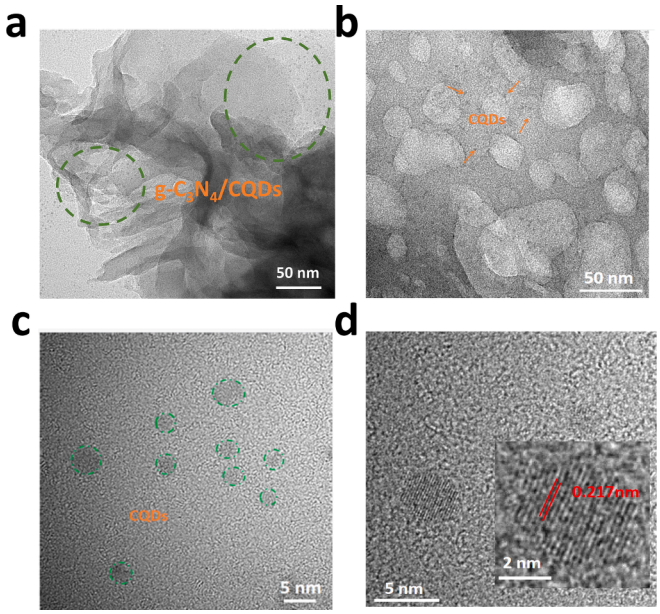

Fig. 5. CQDs TEM characterization of g-C_3N_4 surface.

extend the exposed active sites, enhance surface area, and encourage charge carrier separation [20]. Recently, various morphologies of g-C_3N_4 have been developed, including ultrathin nanosheets [21], three-dimensional (3D) structures [22], porous [23], and hollow tubes [24]. Engineering two-dimensional (2D) ultrathin nanosheets effectively improves catalytic performance. Currently, various methods are used to construct 2D ultrathin nanosheets, such as multi-step thermal oxidation treatment [25], ultrasound-assisted treatment [26], liquid- phase exfoliation [27], and bottom-up methods [28]. In order to increase the surface-active sites of g-C_3N_4, liquid-phase ultrasonic exfoliation is often used as an effective means to obtain ultrathin g-C_3N_4 nanosheets [29]. This method is preferred for the preparation of nanosheets as thin films or composites due to its simplicity, scalability and high effectiveness.

Carbon quantum dot (CQD) is a new type of carbon nanomaterial with sizes ranging from 2 to 10 nm. Due to their distinctive qualities, such as their extremely small size, low toxicity, water solubility, great photochemical stability, and superior electrical conductivity, CQDs have become widely used in electrocatalysis in recent years [30]. In addition, CQDs possess tunable band gaps and unique charge transfer and storage capabilities, making them highly valuable in improving catalytic performance [31]. CQDs can be created using a variety of techniques, which are often categorized as “top-down” or “bottom-up” techniques depending on the carbon source employed [32]. The “top-down” approach entails utilizing strong chemicals to fragment the bulk graphite-like carbon source. However, this method has drawbacks in the areas of choosing raw materials, using complicated instruments, and consuming a lot of energy. In contrast, “Bottom-up” methods such as chemical oxidation, supported synthesis, and hydrothermal/solvent heat treatment offer simpler, cost-effective, and scalable for preparing CQDs. Microwaves, ultrasound, plasma, and microfluidic methods are only a few examples of recent new technologies that have demonstrated various benefits such quick response times, high productivity, and low energy usage. Ultrasonication has emerged as a straightforward and practical choice for making CQDs among these techniques [20]. Small-

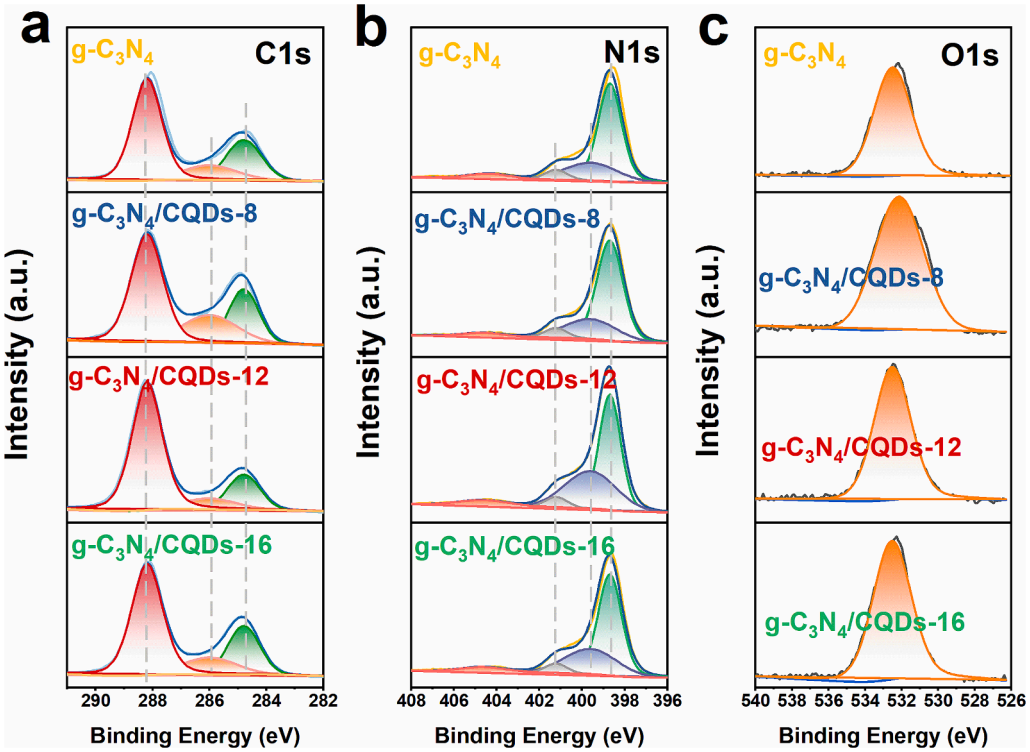

Fig. 6. (a) C 1 s spectra and (b) N 1 s spectra and (c) O 1 s spectra of g-C_3N_4, g-C_3N_4/CQDs-8, g-C_3N_4/CQDs-12, and g-C_3N_4/CQDs-16.

size CQDs can be produced on a wide scale using ultrasonication, which transforms bulk materials into low-dimensional nanostructures. For example, Zhang [33] et al. oxidized 3D bulk g-C_3N_4 using a mixture of concentrated H_2SO_4 and HNO_3 to obtain porous g-C_3N_4, which was then exfoliated 2D nanosheets through hydrothermal treatment in ammonium hydroxide solution. Finally, the nanosheets were sonicated for 6 h to obtain 0D CQDs. Zhuo [34] et al. employed a similar multi-step method to obtain CQDs. In addition to producing extremely thin g-C_3N_4 nanosheets, the ultrasonic synthesis method also causes the fragmentation of macroscopic carbon materials into CQDs, improving catalytic activity.

We used an aided ultrasonic stripping technique to increase the catalytic activity of g-C_3N_4 in light of the remarkable performance of CQDs. In this study, we describe the synthesis of g-C_3N_4/CQDs composites and their significantly enhanced catalytic capabilities for the oxygen reduction process that results in the production of hydrogen peroxide. The g-C_3N_4 nanosheets created during sonication have a higher specific surface area and more active centers than the traditional bulk structure, which improves catalytic activity. Consequently, we successfully synthesized ultrasonically assisted ultra-thin g-C_3N_4 catalysts modified by carbon dots. Then, a thorough investigation was done into the morphology, structure, and electrochemical characteristics of the produced catalysts. The outcomes showed that under particular sonication settings (40 kHz, 120 W, 12 h), the selectivity reached 95%, and the g-C_3N_4/CQDs-12 catalyst produced up to 1466.6 mmol g^{-1} in 12 h at a potential of 0.35 V vs. RHE, which was twice as high as the initial g-C_3N_4 catalyst. Investigated was the catalyst's mechanism for improvement.

2. Experimental section

2.1. Materials synthesis for g-C_3N_4 and instructions for ultrasonic exfoliation

Three carbon- and nitrogen-rich precursors were heated directly to produce the g-C_3N_4 particles. Urea (10 g) was placed in crucibles made of alumina and covered before being heated in a muffle furnace for two hours at a rate of 5 °C per minute. The yellow solid was calcined, then milled and collected, and the resulting powders were marked as g-C_3N_4 [35].

The ultrasonic exfoliation was conducted using the Ultrasonic Wave Cleaner (AK-020, Yuclean). The synthesized materials were exfoliated in 0.1 M KOH under various conditions. We specifically dissolved 20 mg of the g-C_3N_4 sample in 20 mL of 0.1 M KOH solution, resulting in a solution concentration of 1 mg mL^{-1}. Then, we collected the supernatants of the samples after ultrasonic treatment for 8, 12, and 16 h by centrifugation. During this process, the water was changed once every half hour, and the temperature ranged from 20 to 40 ℃. We washed the collected samples with deionized water several times to remove KOH from their surfaces and then dried them at 60 ℃ for 12 h. The samples were identified as being made of g-C_3N_4, g-C_3N_4/CQDs-8, g-C_3N_4/CQDs-12, and g-C_3N_4/CQDs-16. Fig. 1 illustrates the process of g-C_3N_4/CQDs catalyst preparation.

3. Results and discussion

3.1. Morphological and physical characterizations

Firstly, powder X-ray diffraction (XRD) and FT-IR spectroscopy were used to examine the crystal structure and chemical characteristics of the nanosheets at various exfoliation durations (0, 8, 12, and 16 h). The X-ray diffraction is shown in (Fig. 2a), revealing two different diffraction peaks in the samples sonicated for 8 h, 12 h, and without sonication. There is a weak diffraction peak at 13° and a strong diffraction peak at 27°. The diffraction peak at 13° belongs to the in-plane structural mode of tri-s-triazine units and is located at peak (1 0 0) [36]. The peak at 27° is an interlayer stacking of conjugated aromatic rings labeled as peak (0 0 2) of g-C_3N_4 [37]. It is noteworthy that the typical diffraction peaks of CQDs were not found in the g-C_3N_4/CQDs samples, which may be due to the relatively low content of CQDs [38]. It is noteworthy that the intensity of the (0 0 2) peak is significantly reduced after ultrasound treatment, indicating successful delamination of g-C_3N_4 as expected.

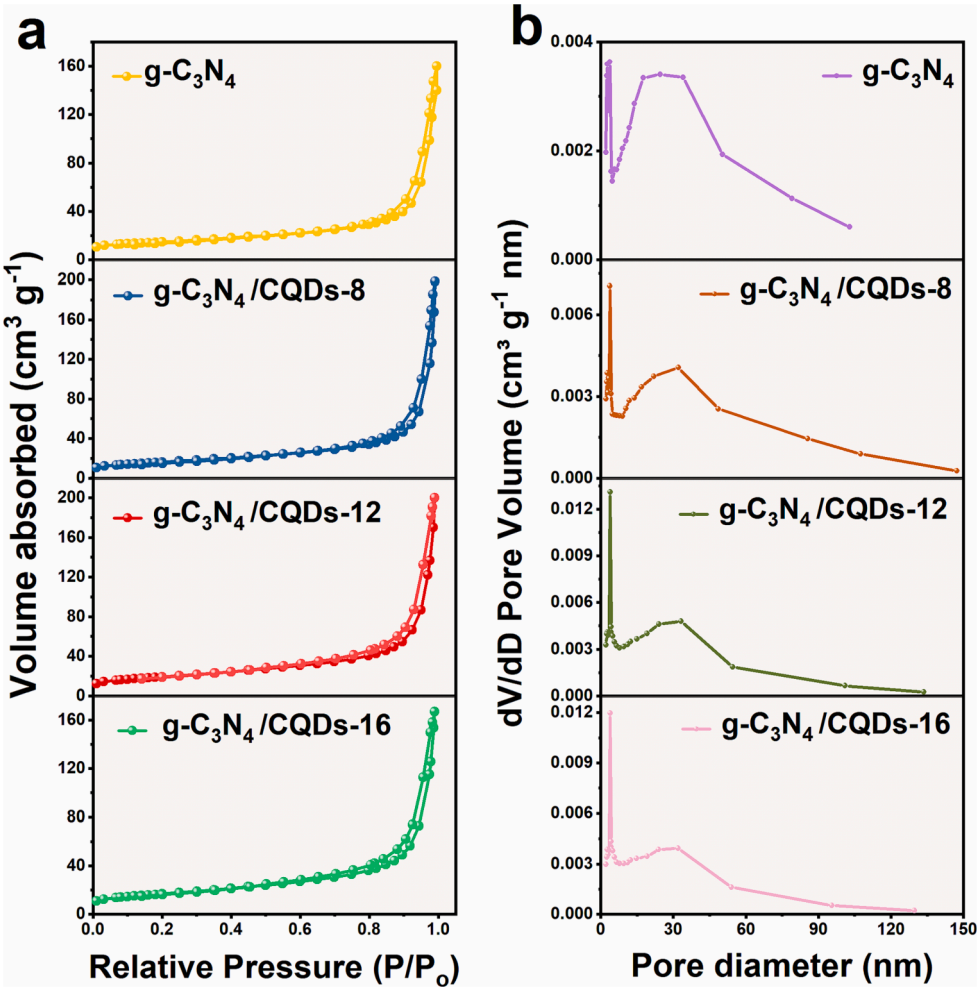

Fig. 7. The N_2 adsorption–desorption isotherms of g-C_3N_4, g-C_3N_4/CQDs-8, g-C_3N_4/CQDs-12, and g-C_3N_4/CQDs-16 and the corresponding BJH pore size distribution curve and pore size distribution are desorbed by isotherms.

Table 1
The BET surface area and pore volume values of g-C_3N_4, g-C_3N_4/CQDs-8, g-C_3N_4/CQDs-12 and g-C_3N_4/CQDs-16.

Sample name	S_{BET} (m^2/g)	V_{pore} (cm^3 g^{-1})	d_{pore} (nm)
g-C_3N_4	50.7731	0.2479	22.0675
g-C_3N_4/CQDs-8	57.1638	0.3067	23.9200
g-C_3N_4/CQDs-12	68.1143	0.3095	19.9051
g-C_3N_4/CQDs-16	59.2565	0.2581	18.7094

When the sonication duration reached 16 h, the peak of the (100) crystal plane near 13° disappeared, indicating that the patterned structure of this crystal plane may have been destroyed after prolonged sonication. As seen in the partially enlarged image of Fig. 2b, the position of the peak was shifted, probably due to the generation of CQDs. Additionally, g-C_3N_4/CQDs-8 and g-C_3N_4/CQDs-12 have peak intensities of (100) and (002) that are much weaker than g-C_3N_4, indicating that the ultrasonic stripping treatment results in the loss of ordered structures in the g-C_3N_4 framework [5].

FT-IR spectra were analyzed to gain more insight into the functional groups of the prepared catalysts, as shown in Fig. 2c. The spike at 807 cm^{-1} is due to the respiration pattern of the tri-s-heptazine or tri-s-triazine unit, whose intensity disappears with increasing sonication time, indicating damage to the basic unit [39]. The stretching vibration of the repeating unit of heptazine is what causes the peaks at 1641, 1570, 1462, and 1412 cm^{-1}, according to the FTIR study of g-C_3N_4. The C-N/C-N stretching vibration mode corresponds to the strong band between 1200 and 1650 cm^{-1}. As the ultrasound period is extended, the peak's intensity in this area similarly decreases, suggesting that the C-N bond was damaged by the ultrasound. With more ultrasound time, the broad peaks between 3000 and 3500 cm^{-1}, which correspond to N-H stretching vibrations, gradually lose intensity and even shift to higher energy levels [40]. The FT-IR research demonstrates that ultrasound had some impact on the g-C_3N_4 structure.

By using SEM, the catalyst's microstructure and surface morphology were investigated. As shown in Fig. 3, the bulk CN shows nanosheets with a large number of irregular aggregates stacked through a laminar structure. After sonication (8, 12, and 16 h) of g-C_3N_4, the native CN was exfoliated, resulting in the formation of fragmented CN nanosheets. All samples have a two-dimensional structure and all have a porous structure brought on by the release of carbon dioxide, ammonia, and water during calcination [35]. After liquid-phase sonication, the size and thickness of g-C_3N_4 become smaller and thinner. According to Fig. 3a–d and e–h, the material develops an increasing amount of pore structure and broken edges as the sonication period goes up. This will provide more active sites and facilitate mass transfer.

The morphology of graphite nitride before and after ultrasonic exfoliation was subsequently characterized using atomic force microscopy (AFM) and transmission electron microscopy (TEM), as shown in Fig. 4. Fig. 4 show g-C_3N_4 without sonication and after 12 h of sonication, respectively. After 12 h of ultrasonic treatment, the graphite carbon nitride changed from 0.862 nm (about three layers) to 0.629 nm

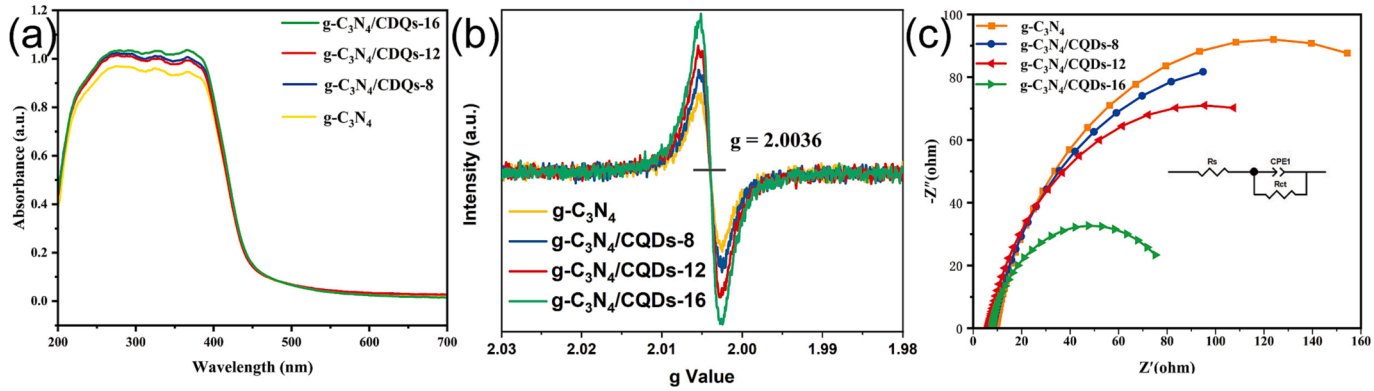

Fig. 8. (a) UV–Vis absorption spectra, (b) EPR spectra and (c) Nyquist plots of EIS for g-C_3N_4, g-C_3N_4/CQDs-8, g-C_3N_4/CQDs-12, and g-C_3N_4/CQDs-16, the inset figure represents the equivalent circuit.

Table 2
Summary of resultant fitting parameters of EIS.

catalyst	Rs/Error (%)	Rct/Error (%)	CPE1-T/Error (%)	CPE1-P/Error (%)
g-C_3N_4	9.478/0.64222	226.7/1.9024	0.00063329/1.9773	0.86836/0.5014
g-C_3N_4/CQDs-8	8.107/0.75911	211.3/3.744	0.0012389/2.5561	0.85078/0.71657
g-C_3N_4/CQDs-12	6.37/0.8413	178.2/2.8464	0.0009864/2.5524	0.85667/0.65994
g-C_3N_4/CQDs-16	7.402/0.63499	82.52/1.4586	0.00097408/2.4414	0.8534/0.60797

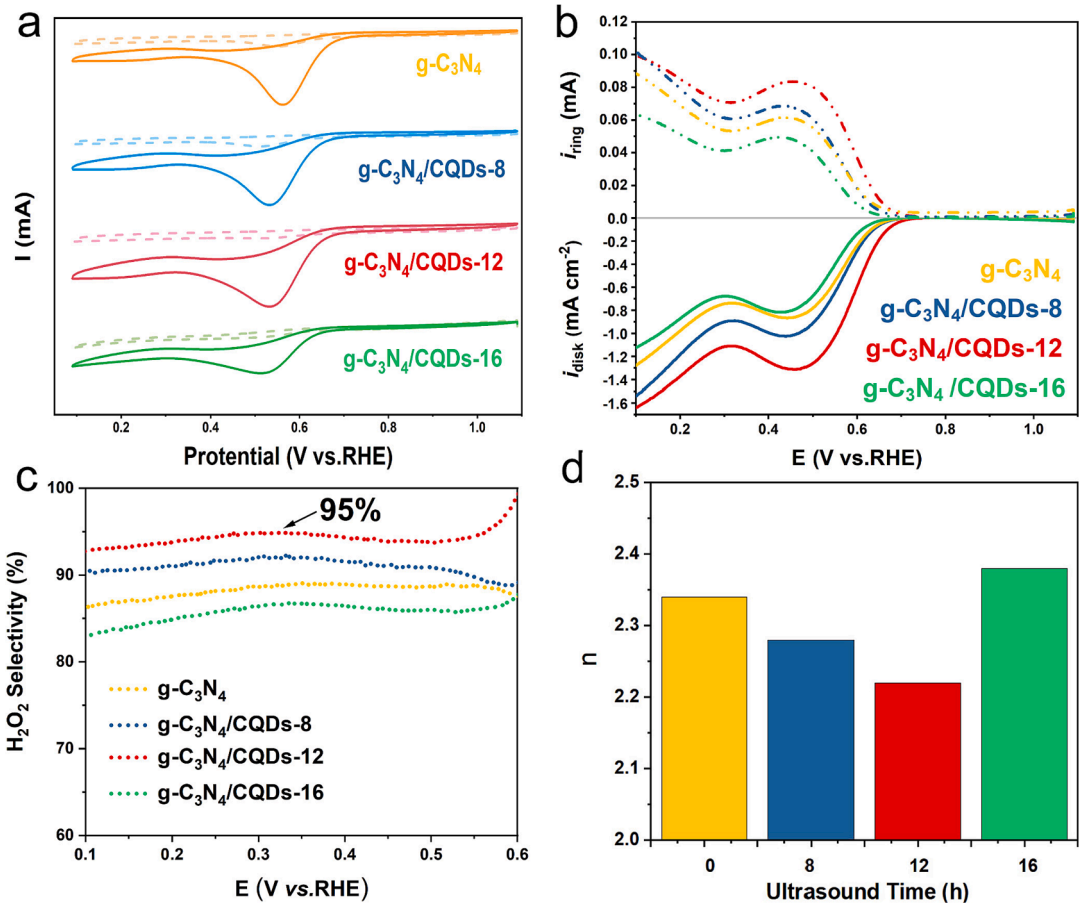

Fig. 9. (a) Cyclic voltammetry (CV) curves saturated with N_2 (dashed line) and O_2 (solid line) at 0.1 M KOH. (b) Polarization curve of catalyst in 0.1 M KOH at 1600 rpm (solid line) and simultaneous hydrogen peroxide detection current (dotted line). (c) Hydrogen peroxide selectivity of g-C_3N_4, g-C_3N_4/CQDs-8, g-C_3N_4/CQDs-12, and g-C_3N_4/CQDs-16 at 0.1 to 0.6 V (vs. RHE). (d) The number of electrons transferred (n) of four materials calculated based on RRDE electrode at 0.4 V vs. RHE.

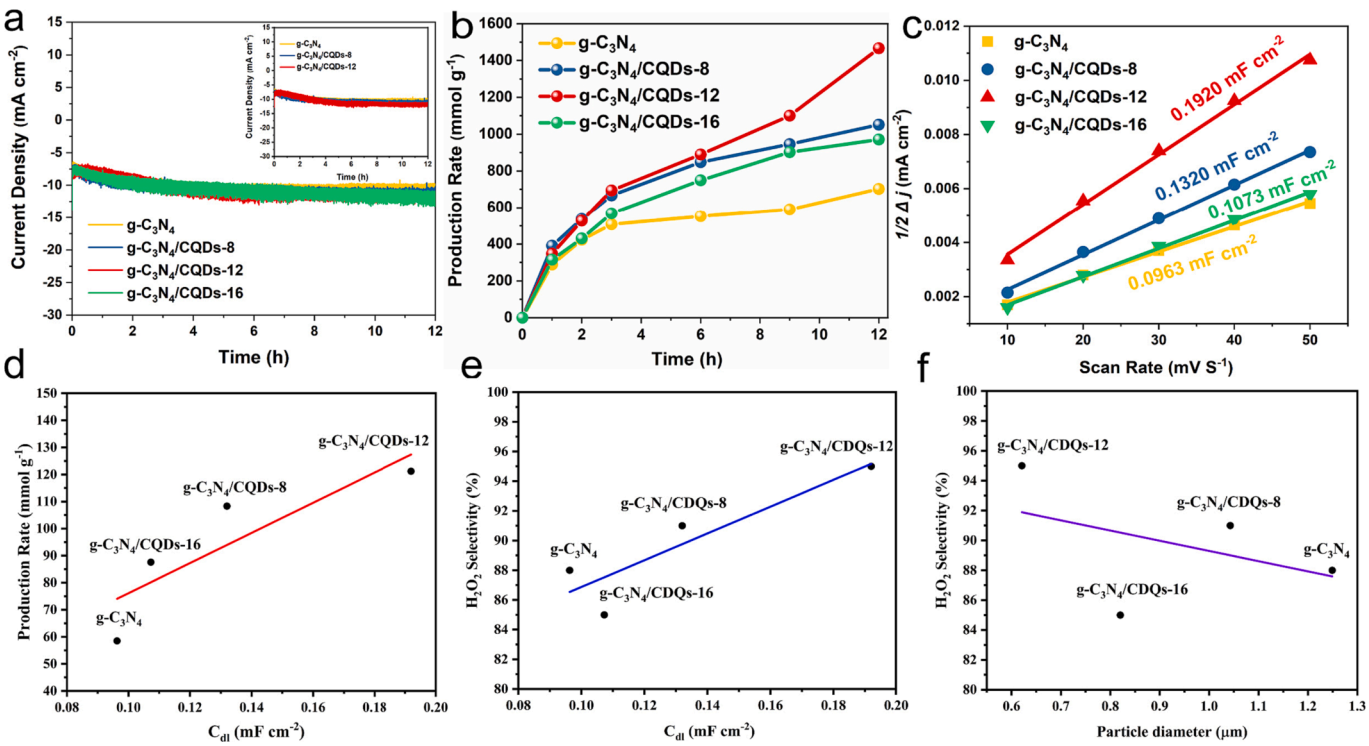

Fig. 10. (a) The stability was measured in 0.1 M KOH at −0.4 V vs. RHE for 12 h. (b) Cumulative hydrogen peroxide production rate at − 0.4 V (vs. RHE) in 0.1 M KOH solution. (c) C_{dl} plots of g-C_3N_4, g-C_3N_4/CQDs-8, g-C_3N_4/CQDs-12, and g-C_3N_4/CQDs-16. (d)Relationship between production rate and C_{dl}. (e) Relationship between H_2O_2 selectivity and C_{dl}. (f) Relationship between particle diameter and H_2O_2 selectivity of three catalysts.

(about two layers). The AFM and TEM showed that the samples were significantly thinner after ultrasonication. The morphology of g-C_3N_4 after ultrasound was also observed using TEM, and Fig. 5(a–b) shows many small quantum dots distributed on g-C_3N_4, which leads to a structure between carbon dots and g-C_3N_4. Fig. 5c shows that the diameter of CQDs is about 2 ∼ 5 nm. The CQDs exhibit a basic morphology and good crystallinity with a planar spacing of around 0.217 nm (Fig. 5d), which can be attributed to the (1 0 1) spacing of graphitic carbon, according to high-resolution TEM image analysis (HRTEM) [41]. AFM and TEM have demonstrated that ultrasonic produces carbon quantum dots while also thinned g-C_3N_4 nanosheets. At the same time, we measured the particle size of four samples with zeta potentiometers (Fig. S1). We found that with the gradual extension of ultrasonic time, when the ultrasonic time is 12 h, the particle size is the smallest, but when the ultrasonic time is further extended to 16 h, the particle size becomes larger, which may be the phenomenon of reunion caused by the long ultrasonic time.

XPS was used to analyze the surface chemistry and oxidation state of the produced catalysts. In Fig. 6 and Fig. S2, the XPS spectra of four samples are displayed. Elements C and N make up the majority of the measured g-C_3N_4 sample. Three peaks can be seen in the C 1 s high-resolution XPS spectra (Fig. 6a) at energies of 284.8, 286.0, and 288.4 eV, respectively. The two peaks at 284.8 and 288.4 eV correspond to the C–C sp^2 hybridized carbon and O=C–O bonds, respectively [42]. The peak at 286.0 eV is probably a C–O bond [43]. Four peaks can be identified in the high-resolution XPS spectra of N 1 s (Fig. 6b), including C=N–C (398.7 eV), tertiary nitrogen N– $(C)_3$ (399.6 eV), N–H (401.2 ev), and π excitation (404.6 eV) [44]. A single O 1 s peak near 532.4 eV, which is associated with the adsorption of carbon dioxide or water on the sample surface, is shown in Fig. 6c. The XPS quantitative results are listed in Table S1.

Fig. 7 depicts the N_2 adsorption–desorption isotherms and Barret-Joyner-Halenda (BJH) pore size distribution curves for the four samples, and Table 1 provides the associated numbers. The weak interaction between adsorbents and adsorbents results in the clear type III behavior that is seen in all samples. The sample exhibits the highest Brunauer-Emmett-Teller (BET) surface area when the ultrasonic duration is 12 h, followed by more than 16 h (about 59 m^2/g) and 8 h (about 57 m^2/g), and the untreated sample (50 m^2/g). In addition, he porosity of the 12 h sample (0.3095 cm^3 g^{-1}) is higher than the other three. It is clear that the ultrasonic-assisted approach enhances the porosity of g-C_3N_4, which is advantageous for the mass transfer of reaction intermediates, as well as the specific surface area of the sample and offers additional reaction sites.

The samples were examined using UV–visible spectroscopy to demonstrate the production of CQDs. As shown in Fig. 8a, the light absorption in the UV–visible region of the sonicated sample is greatly enhanced compared to the unsonicated g-C_3N_4. This is due to the inherent light absorption properties of CQDs, which in turn suggests that sonication of stripped C_3N_4 leads to the production of CQDs [45]. Fig. 8b displays the electron paramagnetic resonance (EPR) spectra of the four materials. The EPR signal steadily grows as ultrasonic time is extended. As a result of a single electron pair on the carbon atom of the heptazine ring in the p-bonded nano-sized cluster, all samples exhibit a Lorentz line with a g value of 2.0036 [25,46]. But in contrast to g-C_3N_4, the sample's substantially greater EPR spin intensity following ultrasonic treatment suggests a higher concentration of unpaired electrons, which is particularly helpful for the photogeneration of active radical pairs that catalyze the reaction. In addition, the great increase in EPR intensity indicates that the density state of the conduction band increases after CQDs species provide electrons [47]. In order to explore the charge transfer ability of introducing CQDs to the ORR process of g-C_3N_4 catalyst, we evaluated the pure g-C_3N_4 and the stripped samples by electrochemical experiments. The electrochemical impedance spectroscopy (EIS) in an O_2 saturated solution was further studied. EIS of the four materials are shown in Fig. 8c. According to the equivalent circuit, Rct is the charge transfer resistance. Rs stands for the solution resistance. CPE is the constant phase element. The fitted data for Rct, Rs and CPE were

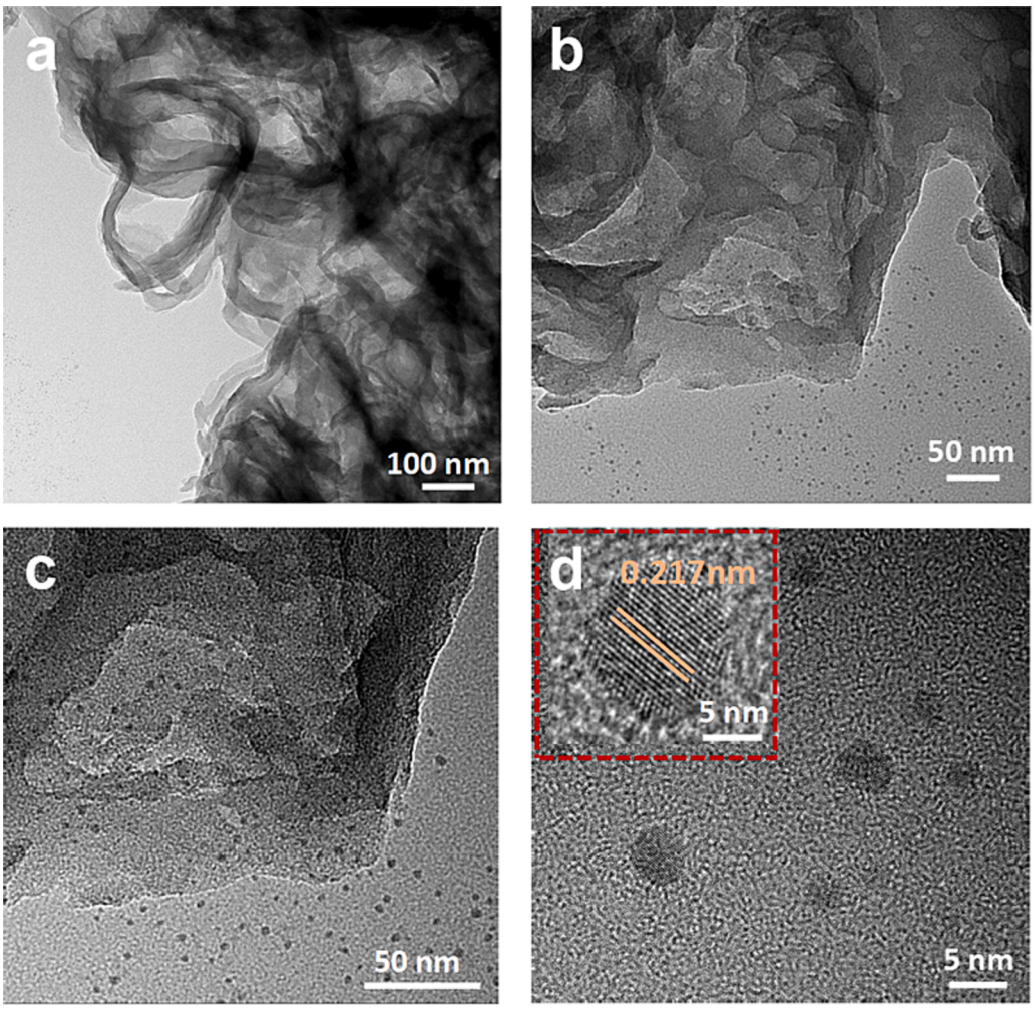

Fig. 11. TEM images of g-C_3N_4/CQDs-12 after 12-hour stability test, (a) Magnification of 100 nm, (b) Magnification of 50 nm, and (c)Magnification of 50 nm, (d) Magnification of 5 nm.

obtained by software analysis (Table 2). It is well known that the smaller the resistivity, the higher the conductivity. As the ultrasound time increases, its Rct value decreases and conductivity increases, indicating that the generation and amount of CDQs is proportional to the ultrasound duration. In Fig. 8c, it can be seen that the diameter of the Nyquist plot of the material decreases significantly with increasing ultrasonication time. This indicates that the resistance of the material after the ultrasonic stripping treatment is lower than that of the pristine g-C_3N_4.The addition of CQDs can be viewed as a workable modification technique to raise the charge transfer rate and electronic conductivity of polymer carbon nitride with an increase in ultrasonic duration [48].

3.2. Electrochemical performance

The CV curves of four samples that were saturated with O_2 and N_2 in 0.1 M KOH are shown in Fig. 9a. In contrast to the nitrogen-saturated electrolyte, the data show a high oxygen reduction peak in the oxygen-saturated electrolyte. With a starting potential of 0.7 V, the Linear Sweep Voltammetry (LSV) curve demonstrates that g-C_3N_4/CQDs-12 exhibits good electrocatalytic performance (Fig. 9b). g-C_3N_4/CQDs-12 has a selectivity of around 95% at 0.35 V vs. RHE, which is higher than that of g-C_3N_4/CQDs-8 (91%), g-C_3N_4 (88%), and g-C_3N_4/CQDs-16 (85%), as shown in Fig. 9c. These findings imply that the $2e^-$ ORR selectivity of g-C_3N_4/CQDs-12 is very high. g-C_3N_4, g-C_3N_4/CQDs-8, g-C_3N_4/CQDs-12, and g-C_3N_4/CQDs-16 had transfer electron numbers of 2.34, 2.28, 2.22, and 2.38, respectively, with g-C_3N_4/CQDs-12 being extremely near to the ideal two-electron reaction (Fig. 9d).

Long-term trials employing the constant voltage approach at −1.28 V and a rotating speed of 1000 rpm were used to examine the stability of the catalyst. As shown in Fig. 10a, all four materials exhibited excellent stability. The long-term yield of hydrogen peroxide for these four catalysts was also measured. After 12 h, the concentration of hydrogen peroxide linearly increased to 0.73 M in the g-C_3N_4/CQDs-12 catalyst in 50 mL of electrolyte (Fig. 10b). g-C_3N_4/CQDs-12 exhibited the highest average hydrogen peroxide yield (121.2 mmol $g^{-1}h^{-1}$) among all of the g-C_3N_4/CQDs catalysts (108.3 mmol $g^{-1}h^{-1}$ for g-C_3N_4/CQDs-8, 87.6 mmol $g^{-1}h^{-1}$ for g-C_3N_4/CQDs-16), which is more than two times that of the original g-C_3N_4 (58.5 mmol $g^{-1}h^{-1}$) (Fig. S3-S4). Additionally, the yield of hydrogen peroxide did not drop noticeably, showing that g-C_3N_4/CQDs-12 has good stability and can fulfill the requirements for long-term hydrogen peroxide synthesis.

By examining the CV curves of the non-Faraday region at various scanning speeds, the electrochemical active surface area (ECSA) of g-C_3N_4, g-C_3N_4/CQDs-8, g-C_3N_4/CQDs-12, and g-C_3N_4/CQDs-16 may be determined (Fig. S5). The electrochemically active surface area of the catalyst is directly reflected by the C_{dl} values. The fact that the C_{dl} of g-C_3N_4/CQDs-12 is 0.192 mF cm^{-2}, approximately twice as high as that of g-C_3N_4 (0.0963 mF cm^{-2}), shows that the material was successfully exfoliated, resulting in a larger surface area with more electrochemically active sites (Fig. 10c). Fig. 10d shows that g-C_3N_4/CQDs-12 also exhibits the maximum yield at a C_{dl} of 0.192 mF cm^{-2}. Moreover, Fig. 10e and f demonstrate that the H_2O_2 selectivity of g-C_3N_4/CQDs catalyst reaches

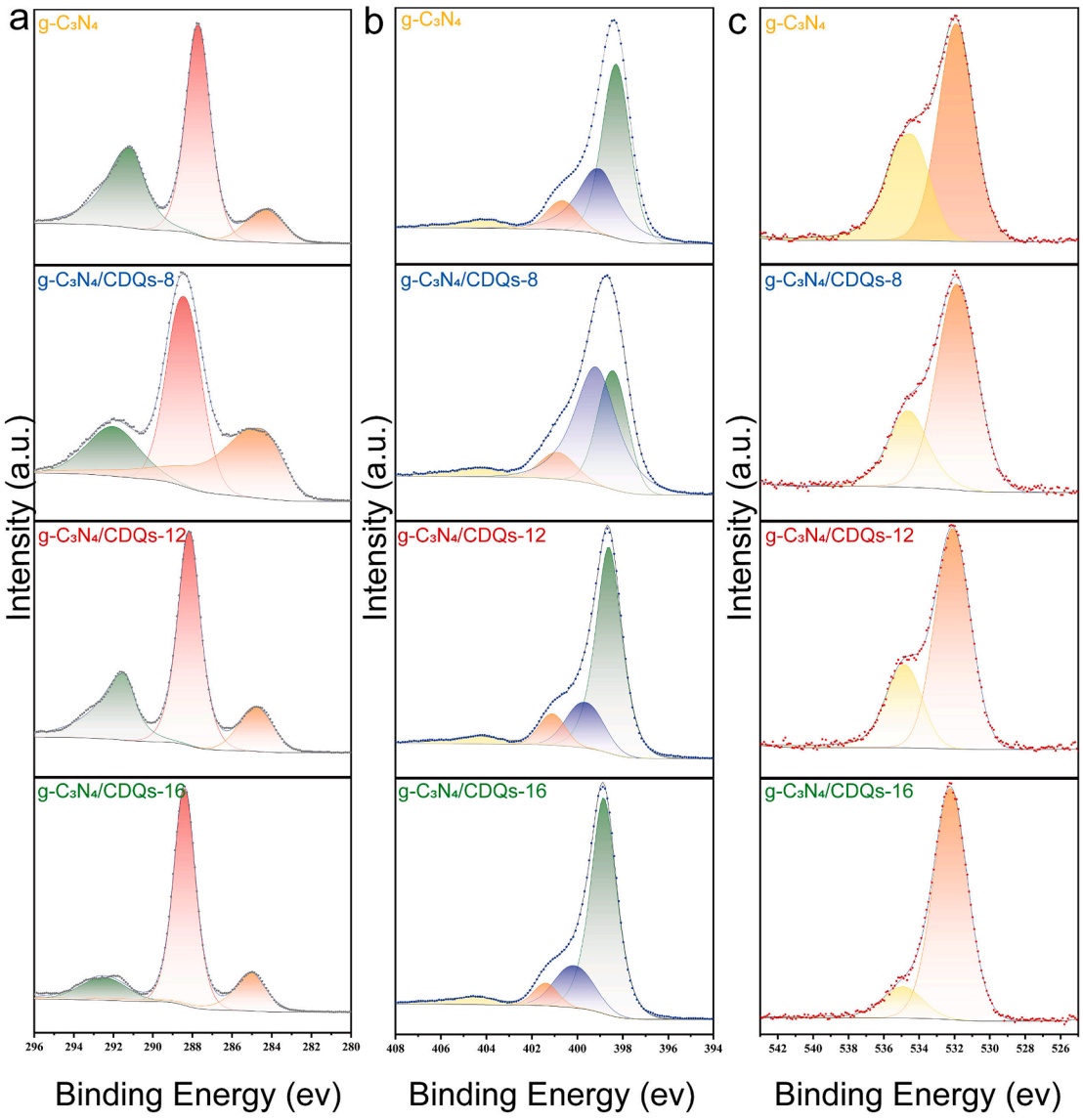

Fig. 12. (a) C 1 s spectra and (b) N 1 s spectra and (c) O 1 s spectra of g-C_3N_4, g-C_3N_4/CQDs-8, g-C_3N_4/CQDs-12, and g-C_3N_4/CQDs-16 after 12-hour stability test.

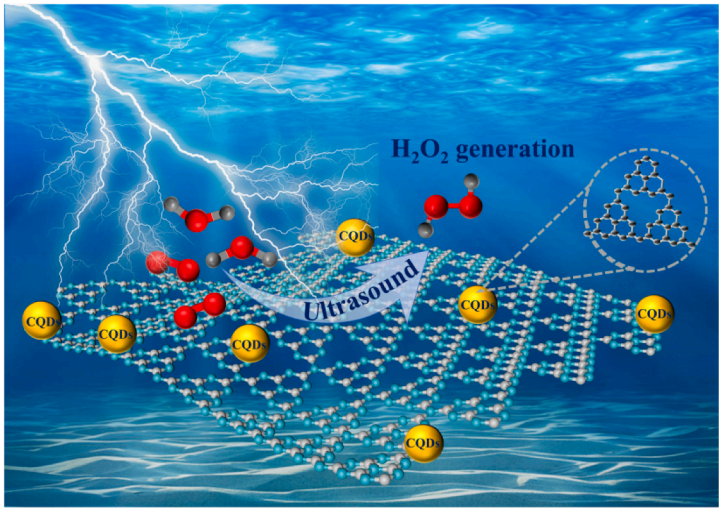

Fig. 13. Mechanism illustration of g-C_3N_4/CQDs catalyst for electrocatalytic production of H_2O_2.

its maximum when the ultrasound time is 12 h, along with the maximum values of C_{dl} and particle diameter. Thus, the ultrasound-assisted technique improves the porosity of g-C_3N_4, which is helpful for the mass transfer of reaction intermediates, in addition to increasing the specific surface area of the sample and providing more reaction sites.

In addition, we characterized the structure and morphology of the samples after the 12-hour stability test. The samples were first analyzed using XRD, as shown in Fig. S6, and it was found that the structure of the samples demained unchange before and after the reaction. Fig. 11a displays the TEM images of the g-C_3N_4/CQDs-12 sample after the 12-hour stability test, and its morphology remained consistent with that before the reaction. Fig. 11(b-d) reveal a large amount of CQDs compounded on the surface of the material. The reaction samples showed good stability by XRD and TEM analysis.

Fig. 12 displays the g-C_3N_4 samples' XPS spectra following stability testing. The measured g-C_3N_4 samples mainly contained C, N, and O elements. The high-resolution XPS spectrum of C 1 s (Fig. 12a) exhibits three peaks at 284.35, 287.68 and 291.13 eV, respectively. The peak at 284.35 eV corresponds the C–C bond [49], the strong peak at 287.68 eV belongs to the C=O bond [50], and the peak at 291.13 eV is associated with the O–C=O group species [51]. Four peaks can be distinguished from the high-resolution XPS spectra of N 1 s (Fig. 12b), including C=N–C (398.28 eV) [52], N−$(C)_3$ (399.02 eV) [53], N–H (400.66 eV) [54], and one belonging to the oxidized N (403.97 eV) [55]. Fig. 12c shows that O 1 s has two peaks, namely the O–C=O bond (531.93 eV) [56] and the adsorbed O_2 (534.49 eV) [57]. Table S2 shows the XPS data of all the samples after the stability test. Based on the XPS comparison before and after stabilization, the samples were more stable. XPS analysis (Fig. S7) suggests that moderate oxidation occurred on the sample surface during the H_2O_2 production process.

3.3. Catalytic mechanism analysis

After 12 h of ultrasonic exfoliation, the hydrogen peroxide production rate of g-C_3N_4/CQDs-12 is around 121.2 mmol $g^{-1}h^{-1}$, which is 2.5 times more than that of untreated g-C_3N_4 (58.5 mmol $g^{-1}h^{-1}$). Its selectivity is increased by around 17%, and its electrocatalytic activity is significantly superior than that of g-C_3N_4, table S3 shows the selectivity of the catalysts. Given that g-C_3N_4/CQDs-12 and g-C_3N_4 have chemical compositions that are similar, we believe that the following factors may be the causes of g-C_3N_4/CQDs-12′s increased electrocatalytic activity. The potential mechanism of H_2O_2 synthesis by the g-C_3N_4/CQDs catalyst is depicted in Fig. 13.

Firstly, the combination of CQDs allows the g-C_3N_4/CQDs-12 catalyst to achieve a high yield and good stability over 12 h in actual H_2O_2 production. CQDs, as a kind of quasi-zero-dimensional carbon, have a very high specific surface area, providing numerous defect sites for heteroatom functionalization and a large number of active sites for heterogeneous electrocatalysis. The effective recombination of CQDs is expected to serve as an efficient carbon matrix for high concentration oxygen-containing active substances in high efficiency $2e^-$ ORR [30]. This work presents an effective and simple strategy for designing efficient metal-free carbon-based catalysts for sustainable H_2O_2 electrosynthesis.

Second, additional active edges, catalytic sites, and channels for electrocatalytic oxygen reduction processes are exposed thanks to the combination of a greater specific surface area and a distinctive porous structure. As is well known, surface electrochemical processes are involved in heterogeneous electrocatalysis, and the catalyst's surface-active sites have a significant impact on the reaction rate. Therefore, a high specific surface area is essential for exposing more active sites and speeding up the electrocatalytic process. The specific surface area and pore size of g-C_3N_4/CQDs-12 significantly bigger, according to SEM and BET characterizations. In addition, the in-plane holes in g-C_3N_4/CQDs-12 are also conducive to the rapid cross-plane diffusion of reaction intermediates and oxygen, significantly accelerating the kinetic electrocatalytic reaction. Therefore, the electrocatalytic activity is enhanced with the increase in specific surface area. However, g-C_3N_4/CQDs-16 falls out of the reference range because of its structural damage caused by long-term peeling.

Thirdly, AFM characterization demonstrates that the ultrasonic-assisted alkali solvent effectviely weakens the Vander Waals force through ultrasonic cavitation, achieving the peeling of g-C_3N_4 layered materials. The material is stripped from the original three layers to two layers. While the bulk form of g-C_3N_4 is normally non-conductive, a single g-C_3N_4 nanocrystal exhibits a clear current. This is so that the essential channel for charge transfer can be provided by the remnant polymerization unit following chemical oxidation, which is coupled to the planar structure by a significant number of hydrogen bonds. The life of the charge is also lengthened as g-C_3N_4′s thickness decreases due to lowered charge motion resistance and faster transmission speed, substantially lowering current loss. Additionally, it reduces the vertical distance of charge flow to the surface, which limits charge accumulation at the nano-sheet surface margins and significantly boosts g-C_3N_4′s catalytic performance and quantum efficiency.

4. Conclusion

In conclusion, we successfully obtained g-C_3N_4/CQDs composites for the first time through ultrasonic methods using g-C_3N_4. By adjusting the exfoliation periods of g-C_3N_4 and testing the ORR activity of each exfoliated sample, we examined the impact of ultrasonic exfoliation. We discovered that the exfoliation and ORR activity of g-C_3N_4 nanosheets were adversely affected by too lengthy (16 h) ultrasonic exfoliation. In order to optimize the conditions, we found that a suspension concentration of 1 mg mL^{-1}, an ultrasonic power of 120 W, a frequency of 40 KHz, and an exfoliation period of 12 h produced the best results. The g-C_3N4/CQDs-12 catalyst performed exceptionally well under these circumstances, with a selectivity of 95% at a potential of 0.35 V vs. RHE, which was almost 17% greater than that of the original g-C_3N_4 catalyst. More so than the initial g-C_3N_4 catalyst, the g-C_3N_4/CQDs-12 catalyst produced up to 1466.6 mmol g^{-1} in 12 h. Furthermore, the introduction of CQDs via sonication facilitated the electrical conductivity of the material, enhancing electron transport, and accelerating the reaction rate. This green strategy effectively achieves a balance between activity and stability in layered materials.

CRediT authorship contribution statement

Yue Wang: Formal analysis, Writing – original draft. **Zhaojing Yang:** Writing – review & editing. **Chengxu Zhang:** Conceptualization, Project administration, Writing – review & editing. **Yuebin Feng:** Validation. **Haodong Shao:** . **Jian Chen:** Formal analysis. **Jue Hu:** Conceptualization, Project administration, Supervision, Writing – review & editing. **Libo Zhang:** Conceptualization, Project administration.

Declaration of Competing Interest

The authors declare that they have no known competing financial interests or personal relationships that could have appeared to influence the work reported in this paper.

Acknowledgements

This research is supported by National Nature Science Foundation of China (Nos. 52364041, 51974141, 51864024, 21862011).

Appendix A. Supplementary data

Supplementary data to this article can be found online at https://doi.org/10.1016/j.ultsonch.2023.106582.

References

[1] J. Xu, X. Zheng, Z. Feng, Z. Lu, Z. Zhang, W. Huang, Y. Li, D. Vuckovic, Y. Li, S. Dai, G. Chen, K. Wang, H. Wang, J.K. Chen, W. Mitch, Y. Cui, Organic wastewater treatment by a single-atom catalyst and electrolytically produced H_2O_2, Nat. Sustain. 4 (2021) 233–241.

[2] J.M. Campos-Martin, G. Blanco-Brieva, J.L.G. Fierro, Hydrogen peroxide synthesis: an outlook beyond the anthraquinone process, Angew. Chem. Int. Ed. 45 (42) (2006) 6962–6984.

[3] Z.W. Seh, J. Kibsgaard, C.F. Dickens, I. Chorkendorff, J.K. Norskov, T.F. Jaramillo, Combining theory and experiment in electrocatalysis: Insights into materials design, Science 355 (2017) eaad4998.

[4] Y. Zhang, Y. Pang, D. Xia, G. Chai, Regulable pyrrolic-N-doped carbon materials as an efficient electrocatalyst for selective O_2 reduction to H_2O_2, New J. Chem. 46 (30) (2022) 14510–14516.

[5] W.-J. Ong, L.-L. Tan, Y.H. Ng, S.-T. Yong, S.-P. Chai, Graphitic Carbon Nitride (g-C3N4)-Based Photocatalysts for Artificial Photosynthesis and Environmental Remediation: Are We a Step Closer To Achieving Sustainability? Chem. Rev. 116 (12) (2016) 7159–7329.

[6] A. Sudhaik, V. Sonu, R. Hasija, T. Selvasembian, A. Ahamad, A.A.P. Singh, P. Khan, P.S. Raizada, Applications of graphitic carbon nitride-based S-scheme heterojunctions for environmental remediation and energy conversion, Nanofabrication 8 (2023) 36.

[7] Y. Wang, X. Wang, M. Antonietti, Polymeric graphitic carbon nitride as a heterogeneous organocatalyst: from photochemistry to multipurpose catalysis to sustainable chemistry, Angew. Chem. Int. Ed. 51 (2012) 68–89.

[8] K. Eid, A. Gamal, A.M. Abdullah, Graphitic carbon nitride-based nanostructures as emergent catalysts for carbon monoxide (CO) oxidation, Green Chem. 25 (2023) 1276–1310.

[9] Z. Teng, W. Cai, S. Liu, C. Wang, Q. Zhang, S. Chenliang, T. Ohno, Bandgap engineering of polymetric carbon nitride copolymerized by 2,5,8-triamino-tri-s-triazine (melem) and barbituric acid for efficient nonsacrificial photocatalytic H2O2 production, Appl. Catal. B Environ. 271 (2020), 118917.

[10] L. Zhou, J. Lei, F. Wang, L. Wang, M.R. Hoffmann, Y. Liu, S.-I. In, J. Zhang, Carbon nitride nanotubes with in situ grafted hydroxyl groups for highly efficient spontaneous H_2O_2 production, Appl. Catal. B Environ. 288 (2021), 119993.

[11] S. Wu, H. Yu, S. Chen, X. Quan, Enhanced Photocatalytic H_2O_2 Production over Carbon Nitride by Doping and Defect Engineering, ACS Catal. 10 (2020) 14380–14389.

[12] X. Zeng, Y. Liu, Y. Kang, Q. Li, Y. Xia, Y. Zhu, H. Hou, M.H. Uddin, T. R. Gengenbach, D. Xia, C. Sun, D.T. McCarthy, A. Deletic, J. Yu, X. Zhang, Simultaneously Tuning Charge Separation and Oxygen Reduction Pathway on Graphitic Carbon Nitride by Polyethylenimine for Boosted Photocatalytic Hydrogen Peroxide Production, ACS Catal. 10 (2020) 3697–3706.

[13] A. Kumar, P. Raizada, A. Hosseini-Bandegharaei, V.K. Thakur, V.-H. Nguyen, P. Singh, C-, N-Vacancy defect engineered polymeric carbon nitride towards photocatalysis: viewpoints and challenges, J. Mater. Chem. A 9 (1) (2021) 111–153.

[14] A. Kumar, P. Raizada, V. Kumar Thakur, V. Saini, A. Aslam Parwaz Khan, N. Singh, P. Singh, An overview on polymeric carbon nitride assisted photocatalytic CO_2 reduction: Strategically manoeuvring solar to fuel conversion efficiency, Chem. Eng. Sci. 230 (2021), 116219.

[15] V.-H. Nguyen, B.-S. Nguyen, Z. Jin, M. Shokouhimehr, H.W. Jang, C. Hu, P. Singh, P. Raizada, W. Peng, S. Shiung Lam, C. Xia, C.C. Nguyen, S.Y. Kim, Q.V. Le, Towards artificial photosynthesis: Sustainable hydrogen utilization for photocatalytic reduction of CO_2 to high-value renewable fuels, Chem. Eng. J. 402 (2020), 126184.

[16] A. Abdelgawad, B. Salah, Q. Lu, A.M. Abdullah, M. Chitt, A. Ghanem, R.S. Al-Hajri, K. Eid, Template-free synthesis of M/g-C3N4 (M = Cu, Mn, and Fe) porous one-dimensional nanostructures for green hydrogen production, J. Electroanal. Chem. 938 (2023), 117426.

[17] Q. Lu, A. Abdelgawad, J. Li, K. Eid, Non-metal-doped porous carbon nitride nanostructures for photocatalytic green hydrogen production, Int. J. Mol. Sci. 23 (2022) 15129.

[18] K. Eid, M.H. Sliem, M. Al-Ejji, A.M. Abdullah, M. Harfouche, R.S. Varma, Hierarchical Porous Carbon Nitride-Crumpled Nanosheet-Embedded Copper Single Atoms: An Efficient Catalyst for Carbon Monoxide Oxidation, ACS Appl. Mater. Interfaces 14 (36) (2022) 40749–40760.

[19] B. Salah, A. Abdelgawad, Q. Lu, A.K. Ipadeola, R. Luque, K. Eid, Synergistically interactive MnFeM (M = Cu, Ti, and Co) sites doped porous g-C3N4 fiber-like nanostructures for an enhanced green hydrogen production, Green Chem. 25 (2023) 6032–6040.

[20] X.Y. Du, C.F. Wang, G. Wu, S. Chen, The Rapid and Large-Scale Production of Carbon Quantum Dots and their Integration with Polymers, Angew. Chem. Int. Ed. 60 (2021) 8585–8595.

[21] X. Bao, M. Liu, Z. Wang, D. Dai, P. Wang, H. Cheng, Y. Liu, Z. Zheng, Y. Dai, B. Huang, Photocatalytic Selective Oxidation of HMF Coupled with H2 Evolution on Flexible Ultrathin g-C3N4 Nanosheets with Enhanced N-H Interaction, ACS Catal. 12 (2022) 1919–1929.

[22] B. Zhou, M. Waqas, B. Yang, K. Xiao, S. Wang, C. Zhu, J. Li, J. Zhang, Convenient one-step fabrication and morphology evolution of thin-shelled honeycomb-like structured g-C_3N_4 to significantly enhance photocatalytic hydrogen evolution, Appl. Surf. Sci. 506 (2020), 145004.

[23] H. Che, C. Liu, G. Che, G. Liao, H. Dong, C. Li, N. Song, C. Li, Facile construction of porous intramolecular g-C_3N_4-based donor-acceptor conjugated copolymers as highly efficient photocatalysts for superior H_2 evolution, Nano Energy 67 (2020), 104273.

[24] H.-X. Fang, H. Guo, C.-G. Niu, C. Liang, D.-W. Huang, N. Tang, H.-Y. Liu, Y.-Y. Yang, L. Li, Hollow tubular graphitic carbon nitride catalyst with adjustable nitrogen vacancy: Enhanced optical absorption and carrier separation for improving photocatalytic activity, Chem. Eng. J. 402 (2020), 104273.

[25] P. Niu, L. Zhang, G. Liu, H.-M. Cheng, Graphene-Like Carbon Nitride Nanosheets for Improved Photocatalytic Activities, Adv. Funct. Mater. 22 (2012) 4763–4770.

[26] F. Cheng, H. Wang, X. Dong, The amphoteric properties of g-C_3N_4 nanosheets and fabrication of their relevant heterostructure photocatalysts by an electrostatic re-assembly route, Chem. Commun. 51 (2015) 7176–7179.

[27] S. Yang, Y. Gong, J. Zhang, L. Zhan, L. Ma, Z. Fang, R. Vajtai, X. Wang, P. M. Ajayan, Exfoliated graphitic carbon nitride nanosheets as efficient catalysts for hydrogen evolution under visible light, Adv. Mater. 25 (2013) 2452–2456.

[28] Y. Xiao, G. Tian, W. Li, Y. Xie, B. Jiang, C. Tian, D. Zhao, H. Fu, Molecule Self-Assembly Synthesis of Porous Few-Layer Carbon Nitride for Highly Efficient Photoredox Catalysis, J. Am. Chem. Soc. 141 (2019) 2508–2515.

[29] D. Lembke, S. Bertolazzi, A. Kis, Single-layer MoS_2 electronics, Acc. Chem. Res. 48 (2015) 100–110.

[30] R. Wang, X. Kong, W. Zhang, W. Zhu, L. Huang, J. Wang, X. Zhang, X. Liu, N. Hu, Y. Suo, J. Wang, Mechanism insight into rapid photocatalytic disinfection of Salmonella based on vanadate QDs-interspersed g-C_3N_4 heterostructures, Appl. Catal. B Environ. 225 (2018) 228–237.

[31] J. Zhang, Y. Ma, Y. Du, H. Jiang, D. Zhou, S. Dong, Carbon nanodots/WO_3 nanorods Z-scheme composites: Remarkably enhanced photocatalytic performance under broad spectrum, Appl. Catal. B Environ. 209 (2017) 253–264.

[32] X. Guan, Z. Li, X. Geng, Z. Lei, A. Karakoti, T. Wu, P. Kumar, J. Yi, A. Vinu, Emerging Trends of Carbon-Based Quantum Dots: Nanoarchitectonics and Applications, Small 19 (2023) 2207181.

[33] Y. Tang, Y. Su, N. Yang, L. Zhang, Y. Lv, Carbon nitride quantum dots: a novel chemiluminescence system for selective detection of free chlorine in water, Anal. Chem. 86 (2014) 4528–4535.

[34] S. Zhuo, M. Shao, S.-T. Lee, Upconversion and Downconversion Fluorescent Graphene Quantum Dots: Ultrasonic Preparation and Photocatalysis, ACS Nano 6 (2) (2012) 1059–1064.

[35] Z. Yang, C. Zhang, Y. Mei, Y. Zhang, Y. Feng, M. Shao, J. Hu, Effect of Nitrogen Species in Graphite Carbon Nitride on Hydrogen Peroxide Production, Adv. Mater. Interfaces 9 (2022) 2201325.

[36] S.C. Yan, Z.S. Li, Z.G. Zou, Photodegradation performance of g-C_3N_4 fabricated by directly heating melamine, Langmuir 25 (2009) 10397–10401.

[37] J. Di, J. Xia, X. Li, M. Ji, H. Xu, Z. Chen, H. Li, Constructing confined surface carbon defects in ultrathin graphitic carbon nitride for photocatalytic free radical manipulation, Carbon 107 (2016) 1–10.

[38] X. Lin, C. Liu, J. Wang, S. Yang, J. Shi, Y. Hong, Graphitic carbon nitride quantum dots and nitrogen-doped carbon quantum dots co-decorated with $BiVO_4$ microspheres: A ternary heterostructure photocatalyst for water purification, Sep. Purif. Technol. 226 (2019) 117–127.

[39] A. Thomas, A. Fischer, F. Goettmann, M. Antonietti, J.-O. Müller, R. Schlögl, J. M. Carlsson, Graphitic carbon nitride materials: variation of structure and morphology and their use as metal-free catalysts, Appl. Surf. Sci. 18 (2008) 4893.

[40] H. Wang, S. Jiang, S. Chen, D. Li, X. Zhang, W. Shao, X. Sun, J. Xie, Z. Zhao, Q. Zhang, Y. Tian, Y. Xie, Enhanced Singlet Oxygen Generation in Oxidized Graphitic Carbon Nitride for Organic Synthesis, Adv. Mater. 28 (2016) 6940–6945.

[41] Y. Wang, X. Liu, J. Liu, B. Han, X. Hu, F. Yang, Z. Xu, Y. Li, S. Jia, Z. Li, Y. Zhao, Carbon Quantum Dot Implanted Graphite Carbon Nitride Nanotubes: Excellent Charge Separation and Enhanced Photocatalytic Hydrogen Evolution, Angew. Chem. Int. Ed. 57 (2018) 5765–5771.

[42] J. Wang, L. Tang, G. Zeng, Y. Deng, H. Dong, Y. Liu, L. Wang, B. Peng, C. Zhang, F. Chen, 0D/2D interface engineering of carbon quantum dots modified Bi2WO6 ultrathin nanosheets with enhanced photoactivity for full spectrum light utilization and mechanism insight, Appl. Catal. B Environ. 222 (2018) 115–123.

[43] J. Cañón, A.V. Teplyakov, XPS characterization of cobalt impregnated SiO2 and γ-Al2O3, Surf. Interface Anal. 53 (2021) 475–481.

[44] J. Liu, T. Zhang, Z. Wang, G. Dawson, W. Chen, Simple pyrolysis of urea into graphitic carbon nitride with recyclable adsorption and photocatalytic activity, J. Mater. Chem. C 21 (2011) 14398.

[45] B. Zhu, X. Li, Y. Wang, N. Liu, Y. Tian, J. Yang, Visible-light-driven photocatalytic degradation of RhB by carbon-quantum-dot-modified g-C_3N_4 on carbon cloth, CrstEngComm 23 (2021) 4782–4790.

[46] J.N. Coleman, M. Lotya, A. O'Neill, S.D. Bergin, P.J. King, U. Khan, K. Young, A. Gaucher, S. De, R.J. Smith, I.V. Shvets, S.K. Arora, G. Stanton, H.-Y. Kim, K. Lee, G.T. Kim, G.S. Duesberg, T. Hallam, J.J. Boland, J.J. Wang, J.F. Donegan, J. C. Grunlan, G. Moriarty, A. Shmeliov, R.J. Nicholls, J.M. Perkins, E.M. Grieveson, K. Theuwissen, D.W. McComb, P.D. Nellist, V. Nicolosi, Two-dimensional nanosheets produced by liquid exfoliation of layered materials, Science 331 (6017) (2011) 568–571.

[47] A. Gupta, V. Arunachalam, S. Vasudevan, Water Dispersible, Positively and Negatively Charged MoS2 Nanosheets: Surface Chemistry and the Role of Surfactant Binding, J. Phys. Chem. Lett. 6 (4) (2015) 739–744.

[48] M. Chhowalla, H.S. Shin, G. Eda, L.-J. Li, K.P. Loh, H. Zhang, The chemistry of two-dimensional layered transition metal dichalcogenide nanosheets, Nat. Chem. 5 (4) (2013) 263–275.

[49] L. Luo, H. Huang, Y. Yang, S. Gong, Y. Li, Y. Wang, W. Luo, Z. Li, Nickel and manganese oxide heterostructure nanoparticles supported by carbon nanotube for highly efficient oxygen evolution reaction catalysis, Appl. Surf. Sci. 575 (2022) 151699.

[50] F. Wang, Q. Hao, Y. Zhang, Y. Xu, W.u. Lei, Fluorescence quenchometric method for determination of ferric ion using boron-doped carbon dots, Microchim. Acta 183 (1) (2016) 273–279.
[51] M.F. Li, Y.G. Liu, G.M. Zeng, S.B. Liu, X.J. Hu, D. Shu, L.H. Jiang, X.F. Tan, X. X. Cai, Z.L. Yan, Tetracycline absorbed onto nitrilotriacetic acid-functionalized magnetic graphene oxide: Influencing factors and uptake mechanism, J. Colloid Interface Sci. 485 (2017) 269–279.
[52] Z. Liu, J. Zhang, Y. Wan, J. Chen, Y. Zhou, J. Zhang, G. Wang, R. Wang, Donor-Acceptor structural polymeric carbon nitride with in-plane electric field accelerating charge separation for efficient photocatalytic hydrogen evolution, Chem. Eng. J. 430 (2022), 132725.
[53] M. Tan, Y. Ma, C. Yu, Q. Luan, J. Li, C. Liu, W. Dong, Y. Su, L. Qiao, L. Gao, Q. Lu, Y. Bai, Boosting Photocatalytic Hydrogen Production via Interfacial Engineering on 2D Ultrathin Z-Scheme ZnIn2S4/g-C3N4 Heterojunction, Adv. Funct. Mater. 32 (14) (2022).
[54] Z. Zhao, Y. Guo, T. Zhang, J. Ma, H. Li, J. Zhou, Z. Wang, R. Sun, Preparation of carbon dots from waste cellulose diacetate as a sensor for tetracycline detection and fluorescence ink, Int. J. Biol. Macromol. 164 (2020) 4289–4298.
[55] H. Li, X. Li, J. Ding, X. Li, W. Zhao, M. Liu, W. Yu, Hierarchical nano-porous biochar prepared by a MgO template method for high performance of PNP adsorption, New J. Chem. 45 (2021) 7332–7343.
[56] X. Qian, F. Li, L. Jin, MOF drived MnO/N–C/CNT composite and its modified separator for advanced Li–S battery, Micropor. Mesopor. Mater. 329 (2022), 111558.
[57] Y. Jiang, F. Li, Y. Liu, Y. Hong, P. Liu, L. Ni, Construction of TiO_2 hollow nanosphere/g-C_3N_4 composites with superior visible-light photocatalytic activity and mechanism insight, J. Ind. Eng. Chem. 41 (2016) 130–140.